# Toward Polarization-Enabled Wildfire Detection

Wildfire season in the United States is becoming longer with more intense fires. The National Interagency Fire Center has reported an annual increase in the burned area of 800 $km^2/yr$ since 1980 [1]. Currently, widespread techniques for detecting wildfires rely on humans in watchtowers, satellite imagery, and strategically placed sensors or cameras. These techniques have shown the ability to detect wildfires within 24 hours or as short as 1 minute after ignition. However, there are several disadvantages to these methods. Watch towers and satellites are limited in spatial coverage and require the wildfire to be large enough for detection at large distances. Sensors and cameras offer increased spatial coverage, but require that the wildfire be within the field of view of the camera or the coverage of the sensor [2]. More robust detection methods are being explored to find solutions that are not dependent on the wildfire being within the field of view.

The positions of the four sky polarization neutral points (points of unexpected random polarization) are changed by the presence of aerosols (e.g. smoke, dust) anywhere within the sky dome [3, 4, 5, 6]. So, monitoring their positions offers a promising tool for wildfire detection [1, 7]. However, more studies are needed to test the validity of this prospect. This comprehensive exam explicates the fundamental optical physics principles of sky polarization neutral points and then showcases the optical engineering and image science tools needed to obtain an image of the Babinet neutral point.

## Optical Physics: Sky Polarization

When randomly polarized Sunlight enters our atmosphere, the interaction with air molecules results in the radiation of polarized light. This produces a pattern of polarization that is tangential to the Sun, except for the presence of four polarization singularities, known as neutral points. This section defines polarization and then discusses the optical mechanisms of sky polarization.

Light propagates as a transverse wave, with the electric field vector oscillating in a plane perpendicular to the direction of propagation. This transverse nature of light can be explained by Maxwell's equations. In the case of a plane wave traveling along the z-direction, the charge-free condition $\nabla \cdot \mathbf{E} = 0$ and $\nabla \cdot \mathbf{B} = 0$ implies that $\partial E_z / \partial z = 0$, which means that changes in the electric field occur in the directions perpendicular (along $x$ or $y$) to the propagation direction ($z$), thus

confirming the transverse nature of light. Similarly, the magnetic field is transverse, perpendicular to both the direction of propagation and the electric field.

Within the transverse plane, at any fixed point in time, the electric field can be decomposed into orthogonal components, often denoted as $\mathbf{E} = E_{\hat{x}} + E_{\hat{y}}$. This composite $\mathbf{E}$ vector traces out an ellipse known as the polarization ellipse. This ellipse represents the path followed by the tip of the electric field vector as it oscillates over time, and is referred to as the polarization of the wave. The orientation and shape of this ellipse are determined by the relative magnitudes and phases of $\mathbf{E}_{\hat{x}}$ and $\mathbf{E}_{\hat{y}}$, which can be derived from the initial conditions of the plane wave equation, ensuring that the real part of the field oscillates in both time and space. The polarization state of a wave can be linear ($\gamma_{\hat{x},\hat{y}} = 0°$ or $180°$), circular ($|E_{\hat{x}}| = |E_{\hat{y}}|$, $\gamma_{\hat{x},\hat{y}} = 90°$ or $-90°$), or elliptical, with all other cases falling into the latter category [8, 9]. The orientation of electric field oscillations can have no preferential orientation (*i.e.*, randomly polarized), oscillate in many orientations with a tendency towards a given orientation (*i.e.*, partially polarized), or only oscillate in a specific orientation (*i.e.*, polarized). Sunlight does not have a preferential polarization state and is considered randomly polarized. The interactions of Sunlight with Earth's atmosphere create polarized skylight through the process of Rayleigh scattering [10].

Rayleigh scattering occurs when the incident wavelength ($\lambda$) is much larger than the diameter of the scattering object ($d$). When Sunlight interacts with the dielectric air molecules the air molecule becomes a radiating dipole source. The intensity of the scattered radiation ($I$) is given by,

$$I = I_0 \frac{8\pi^4 \alpha^2}{\lambda^4 R^2} \left( \frac{n^2 - 1}{n^2 + 2} \right)^2 \left( 1 + \cos^2\theta \right) . \tag{1}$$

Here, $I_0$ is the incident intensity in $Wm^{-2}$, $R$ is the distance from the scattering particle to the point of observation in $m$, $\alpha$ is the polarizability of the scattering particle in $m^3$, $n$ is the refractive index of the medium surrounding the particle, $\theta$ is the scattering angle, the angle between the incident light and direction of observation [11, 12]. Thus, Equation 1 shows that $I$ is inversely proportional to $\lambda^4$ and decreases over $R^{-2}$. In the atmosphere, the $\lambda$ and $R^{-2}$ relationships result in diffuse skylight which appears predominantly

blue during daylight hours and more red and orange during sunrise and sunset [13, 11].
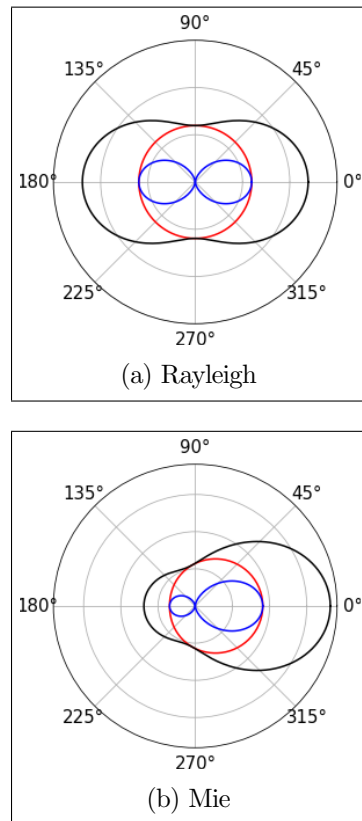


(a) Rayleigh



(b) Mie

Figure 1: Scattering phase function for (a) Rayleigh and (b) Mie (m = 1, $n_a$ = 1.5) plotted over scattering angle, $\theta$. $I$ is shown in black, $I_\parallel$ in blue, and $I_\perp$ in red.

Rayleigh scattering is anisotropic, meaning the intensity and polarization of the scattered light vary over the scattering angle. From Equation 1 the variation in intensity follows $I\alpha(1+cos^2(\theta))$. Plotting $I$ over $\theta$ yields the plot shown in Figure 1a, known as the scattering phase function. The polarization state is defined from the scattering plane, the plane containing the direction of incident light, and the plane containing the direction of observation. Then, the intensity can be broken into two components, $I_\perp$ and $I_\parallel$. The parallel component is proportional to $cos^2(\theta)$ and the perpendicular component is independent of the scattering angle, as shown in Figure 1a. When $I_\perp = I_\parallel$, the scattered light is randomly polarized at $\theta = 0°$ or $180°$. When $I_\parallel$ drops to zero, the scattered light is fully perpendicularly polarized, at $\theta = 90°$ or $270°$. The scattered light is partially polarized at all other values of $\theta$, Figure 1a [11]. The intensity and polarization of Rayleigh scattering within the atmosphere were formulated into the Rayleigh sky model by Lord Rayleigh in 1871. The Rayleigh sky model demonstrates that the polarization signature of the sky follows Rayleigh scattering expectations, with fully polarized light that is perpendicular to the scattering plane 90° from the Sun, see Figure 2c [13]. However, this model did not account for four polarization singularities that disrupt the expectation of partially polarized light above and below the Sun and above and below the anti-Sun [4].

These singularities or *neutral points* are named Babinet (above the Sun), Brewster (below the Sun), Arago (above the anti-Sun), and The Fourth (below the Sun); see Figure 2d [4, 3]. Other than the fourth, the neutral points are named after the scientist who observed or theorized them. At these neutral points, the skylight is randomly polarized. These singularities are the result of multiple scattering of polarized skylight. As shown in Figure 1a, $I_\parallel$ is predominantly forward
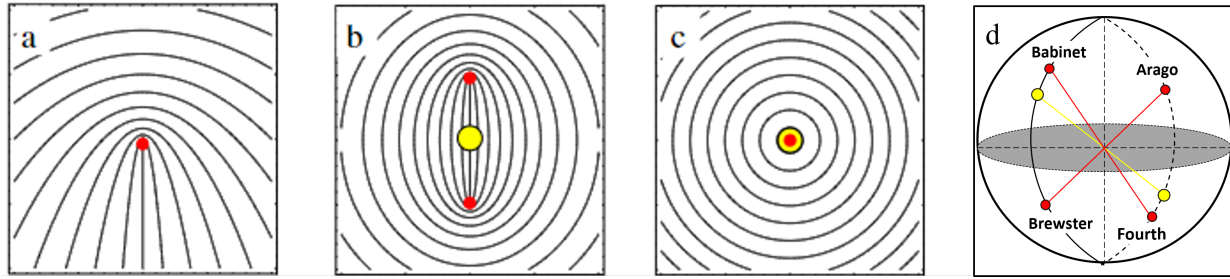
Figure 2: Contour map of polarization orientation relative to the Sun or Anti-Sun (yellow dot), in (a) one polarization singularity (red dot), in (b) the polarization orientation around two singularities, and (c) hypothetical absence of singularities (d) graphical depiction of the four neutral points. [4, 14]

and backscattered. When the polarized skylight is multiply scattered in the atmosphere, the $I_\parallel$ component of this new scattered radiation, which will be denoted with a prime, $I_\parallel'$, is sent back towards the Sun and anti-Sun. Between the Sun and the neutral point $I_\parallel'$ is greater than $I_\perp$, resulting in a net parallel polarization state, until canceling out at the neutral point, before $I_\perp$ again dominates and the polarization signature returns to Rayleigh expectations; see Figure 2a,b [4, 13]. The scattering angles over which $I_\parallel'$ is greater than $I_\perp$, i.e. the position of the neutral point from the Sun, will depend on wavelength and atmospheric conditions [14, 3, 15]. So far, research has determined that the precise locations of these neutral points are between 15-30° above or below the Sun. These observations have been conducted using fish eye or wide field of view lenses, which image the entire sky dome at the cost of decreased spatial resolution and therefore can only report the location of the neutral point within 1.0° [3, 16].

When particulates are suspended in the atmosphere, otherwise known as aerosols, they will scatter light according to Rayleigh scattering when $(\lambda >> d)$ or according to Mie scattering when $(\lambda \approx d)$, or larger, but not yet converging to geometric optics approximations. Mie scattering is typically reserved for approximating aerosols as spherical scattering objects. The scattering phase function from a Mie scattering event is far more complex and involves directly solving Maxwell's equations with solutions varying due to the index of refraction of the scattering object $(n_a)$ and the size parameter, $m = \pi d / \lambda$. This differs from the scattering phase function of Rayleigh scattering, Equation 1, which is not dependent on the index of refraction of the scatter or the size of the scatterer. The lack of these dependencies is because Rayleigh is an approximation of

Mie scattering [11, 12]. The Mie scattering phase function relationship to $\lambda$ is less pronounced and does not have a simple power-law proportion. There are multiple solutions for Mie scattering phase functions, but the scattered intensity is typically highest in forward scattering, as shown in Figure 1b. So, the intensity of the polarized scattered radiation is weaker compared to Rayleigh scattering[11]. When the skylight undergoes Mie scattering in addition to multiple scattering, the intensity of $I'_\parallel$ will increase or decrease, affecting the position of the neutral point.

Aerosols vary widely in size and index of refraction, so each type of aerosol will scatter light differently. In the case of wildfire smoke, the predominant aerosols are black carbon and organic aerosols ranging in size from 1-1000 nm [17]. Since UV and visible wavelengths are on the same order of these particle sizes, Mie's solution or the Rayleigh approximation can be used to describe the scattering. The effects of smoke aerosols on the position of the neutral point have never been studied, nor for any other type of aerosol, but deviations in the neutral point position have been reported under different amounts of aerosol loading (the mass concentration of aerosols) and cloud cover [14, 5, 6, 15]. However, these studies have not specified how much the neutral point deviates under different aerosol loading due to low quantities of data [6].

## Optical Engineering: Instrument Development

Measuring the Babinet neutral point requires an instrument capable of measuring both radiometry and polarization, known as a polarimeter. This discussion will focus on a division-of-time (DoT) linear Stokes imaging polarimeter, the Ultraviolet Linear Stokes Imaging Polarimeter (ULTRASIP).

The Stokes parameters are derived from the time-average of the polarization ellipse $\langle E_x(z,t)E_y(z,t)\rangle$ $=\lim_{T\to\infty}\frac{1}{T}\int_0^T E_x(z,t)E_y(z,t)dt$, where $T$ is the total averaging time. Then the Stokes parameters of units $W/m^2$ are defined in a vector, $\mathbf{S}$, as,

$$\mathbf{S}=\begin{pmatrix}S_0\\S_1\\S_2\\S_3\end{pmatrix}=\begin{pmatrix}|E_x|^2+|E_y|^2\\|E_x|^2-|E_y|^2\\2|E_x||E_y|cos(\theta_{\hat{x},\hat{y}})\\2|E_x||E_y|sin(\theta_{\hat{x},\hat{y}})\end{pmatrix}=S_0\begin{pmatrix}1\\cos(2\chi)cos(2\psi)\\cos(2\chi)sin(2\psi)\\sin(2\chi)\end{pmatrix}=\begin{pmatrix}P_0+P_{90}\\P_0-P_{90}\\P_{45}-P_{135}\\P_{RHC}-P_{LHC}\end{pmatrix}. \qquad (2)$$

Here, $S_0$ is the total intensity, $S_1$ indicates the prevalence of x-component intensity over y-component intensity, $S_2$ is the counterclockwise diagonal prevalence over the clockwise diagonal intensity, and $S_3$ refers to the intensity of right-handed circular (RHC) polarization prevalence over the left-hand circular (LHC) polarization. In the context of atmospheric polarization, the latter is considered negligible, and hence discussions on atmospheric polarization only consider the linear Stokes parameters $(S_1, S_2)$.

Within a linear Stokes polarimetric imaging system, the Stokes parameters are determined by analyzing flux images taken at various polarizer orientations, $\phi$ ($0 \leq \phi \leq 360$), and the resulting flux measurements are denoted as $P_\phi$. To obtain the complete linear Stokes vector, at least three linearly independent measurements are required. For optimal polarization measurements, the most commonly chosen $\phi$ values are $\phi = [0, 45, 90, 135]$. This selection is based on considerations of geometric interpretation and hardware practicality. Each measured flux image captures different aspects of the electric field such that $P_0 = |E_x|^2$, $P_{90} = |E_y|^2$, $P_{45} = E_x E_y^*$, and $P_{135} = E_x^* E_y$. The Stokes parameters are used to define a polarization state with two quantities: degree of linear polarization (DoLP) and angle of linear polarization (AoLP).

DoLP represents the ratio of polarized light to total intensity, or the *randomness* of the polarization state, with values ranging from 0 (randomly polarized) to 1 (fully polarized). DoLP is calculated from the Stokes parameters using the formula $\text{DoLP} = \frac{cos(2\chi)}{S}\Big|_0 = \frac{\sqrt{S_1^2 + S_2^2}}{S_0}$. AoLP describes the orientation of the polarization state and depends on the choice of the reference plane. AoLP is defined as counter-clockwise looking into the beam [2]. In sky polarization measurements, the common reference planes are the meridian plane (spanning the zenith and the view vector) and the scattering plane (spanning the Sun illumination vector and the view vector)[2]. AoLP is determined from the Stokes parameters using the formula $\text{AoLP} = \frac{1}{2}\arctan\left(\frac{S_2}{S_1}\right)$ and is equal to $\psi$. Typically, the range of AoLP is constrained to $0° \leq AoLP \leq 180°$, as AoLP remains unchanged under $180°$ rotations.

ULTRASIP uses a rotational motor to rotate a linear polarizer and obtain three linearly independent measurements (four images), making it a division-of-time polarimeter. The sensor

for the UV imaging system is the SONY IMX487 Back-Illuminated Complementary Metal-oxide-semiconductor (CMOS) sensor housed in an Alvium camera (1800 U-812 UV). CMOS sensors individually convert light to each pixel, offering faster processing than a charge-coupled device type sensor (CCD) but sacrificing uniformity, sensitivity, and increasing fixed-pattern noise. However, pixel-level processing reduces blooming and increases the dynamic range. This makes CMOS sensors ideal for sky imaging, as they can handle high light levels without blooming, ensuring clearer images. Additionally, their fast readout speed is advantageous for tracking dynamic atmospheric features. The SONY IMX487 sensor is fabricated for optimum quantum efficiency (QE) in the UV, specified with a maximum QE in the UV of 50.75% at 400 nm and QE above 30% from 220 nm to 400 nm [18]. A 355 nm $\pm$ 10 nm hard-coated bandpass filter is placed in front of the sensor. Then, a 25 mm lens with a variable aperture is mounted in front of the camera and sensor. The lens elements are made from fused silica, which is highly transmissive in the UV, with transmittance above 85% across the UV spectrum. When used with the Alivium camera, the field of view (FOV) is 17.68°, or 0.0062° per pixel. The internal iris on the lens allows for f-numbers ($f/\#$) ranging from $f/2.8$ to $f/16$.

For a DoT polarimeter that measures linear polarization states, $\phi = [0,45,90,135]°$ the output fluxes are given by, $\mathbf{P} = \mathbf{WS} = [P_0, P_{45}, P_{90}, P_{135}]^\dagger$. Here $\mathbf{W}$ is a $4 \times 3$ matrix, the rows are the response of each polarizer orientation. The rows are not linearly independent because only the first three linear Stokes components of Equation 2 are measured. The W-matrix of a polarimeter is estimated by polarimetric calibration. The quality of $\mathbf{W}$ is affected by: the spectrally-dependent extinction ratio of polarizers, total attenuation of the system, stray light and surface scattering, and field-dependent polarization aberrations.

ULTRASIP measures an image at a given polarizer orientation, denoted $[P_\phi]_{l,m}$ for an $[l,m]$ pixel coordinate. The DoLP and AoLP images are then calculated from the $P_\phi$ images; see Figure 3. The neutral point images show DoLP continuously decreasing towards the neutral point, Figure 3a, singularity and AoLP is rapidly processing about the singularity, Figure 3b. The apparent size of the neutral point, in a DoLP or AoLP image, is determined by both polarimetric and
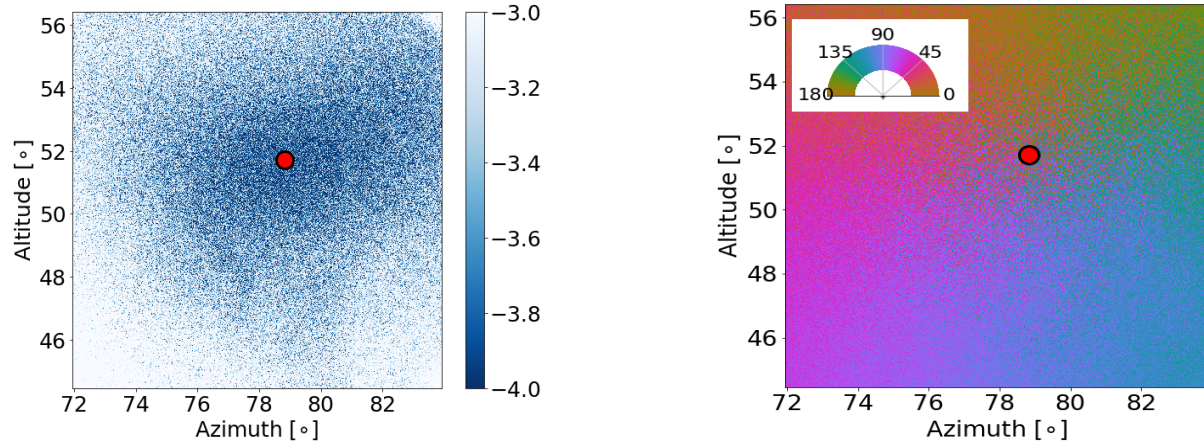
(a) Log of neutral point degree of polarization [%]

(b) Neutral point angle of linear polarization [°]

Figure 3: In (a) log(DoLP) and in (b) AoLP [°] of Babinet neutral point taken on April 3rd, 2024 with a bandpass of 355nm $\pm$ 10nm. The variance increases towards the neutral point as the DoLP goes to zero and the AoLP varies rapidly. Solar (Azimuth, Altitude)= (77.14°, 29.64°). The red dot is the estimated neutral point location (78.82°, 51.70°). Position estimation methods are discussed in the Image Science section.

radiometric efficiencies.

## Image Science: Neutral Point Position Estimation

The neutral point in a DoLP gradient is characterized by a DoLP value of zero, where the AoLP transitions between orthogonal polarization states on opposite sides of the neutral point, as seen in Figure 3. This phenomenon occurs because, at the exact location of the neutral point, all pairs of orthogonal polarization states are equal in magnitude and incoherently sum to unpolarized. In the ideal limit of infinitesimal polarimetric and spatial resolution, ULTRASIP would measure $P_0 = P_{90}$ and $P_{45} = P_{135}$. In practice, the DoLP measurement variance increases as the signal depolarizes, see Figure 3a. The features in an AoLP image offer a visual assessment of statistical significance. The AoLP image becomes full of high-frequency variation when the DoLP is lower than the polarimetric resolution [19].

Instead of a pixel-wise search for minimum DoLP, the expected polarization pattern within an image provides an estimation method of the neutral point's location. The raw $P_\phi$ measurements are used instead of non-linear DoLP and AoLP transforms. The statistics of $P_\phi$ are expected to be Gaussian and simply averaging pixel values forms unbiased estimates of the observation.

(a) $P_0/S_0$      (b) $P_{90}/S_0$      (c) $P_{45}/S_0$      (d) $P_{135}/S_0$
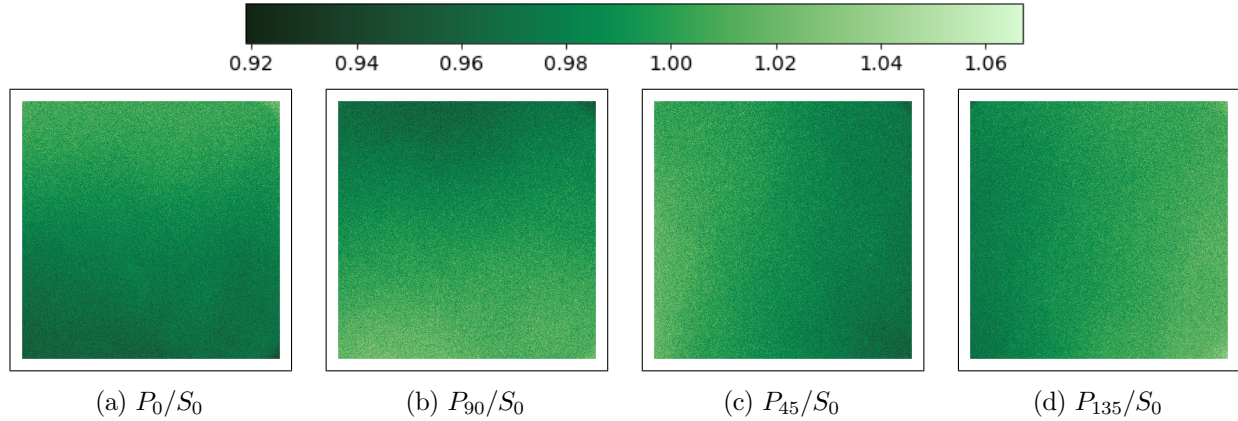
Figure 4: The normalized polarized flux images from same dataset as in Figure 3. Note that $P_0$ and $P_{90}$ are approximately invariant along the rows and $P_{45}$ and $P_{135}$ along the columns.

Since DoLP is a non-linear function of the flux images the statistics are non-Gaussian and the sample mean is biased. AoLP increases in variance as the DoLP decreases. At the exact location of the neutral point when DoLP=0 the AoLP is undefined. The neutral point position becomes challenging to discern from an AoLP image alone, see Figure 3b. In contrast, $P_\phi$ images contain full polarimetric information with an approximately normal noise distribution. Therefore, the neutral point position is estimated from sample averages of flux images.

At the neutral point, where $P_0 = P_{90}$ and $P_{45} = P_{135}$, the orthogonal flux gradients have opposing directions. This behavior is illustrated in the measured flux images (see Figure 4). To identify the location within the image where the orthogonal fluxes are equal, the normalized average flux for each $P_\phi$ is calculated using Equation 3, and orthogonal fluxes are plotted together. The flux images are normalized by the total intensity to account for non-uniformity within the image. For $P_0$ and $P_{90}$, the flux gradient is greatest along the image columns and minimal along the rows. Conversely, for $P_{45}$ and $P_{135}$, the gradient is greatest along the rows and minimal along the columns, as shown in Figure 4. The average flux along the invariant directions are calculated and normalized according to,

$$\bar{r}_\phi = \frac{1}{J}\sum_{j=0}^{J}\left[\frac{P_\phi}{S_0}\right]_{lj} \quad \phi \in [0°, 90°], \qquad \bar{c}_\phi = \frac{1}{L}\sum_{l=0}^{L}\left[\frac{P_\phi}{S_0}\right]_{lj} \quad \phi \in [45°, 135°]. \tag{3}$$

A linear fit to these averages for the rows and columns is shown in Figure 5. The intersection

(a) Plot of $\bar{r}_0$ and $\bar{r}_{90}$       (b) Plot of $\bar{c}_{45}$ and $\bar{c}_{135}$
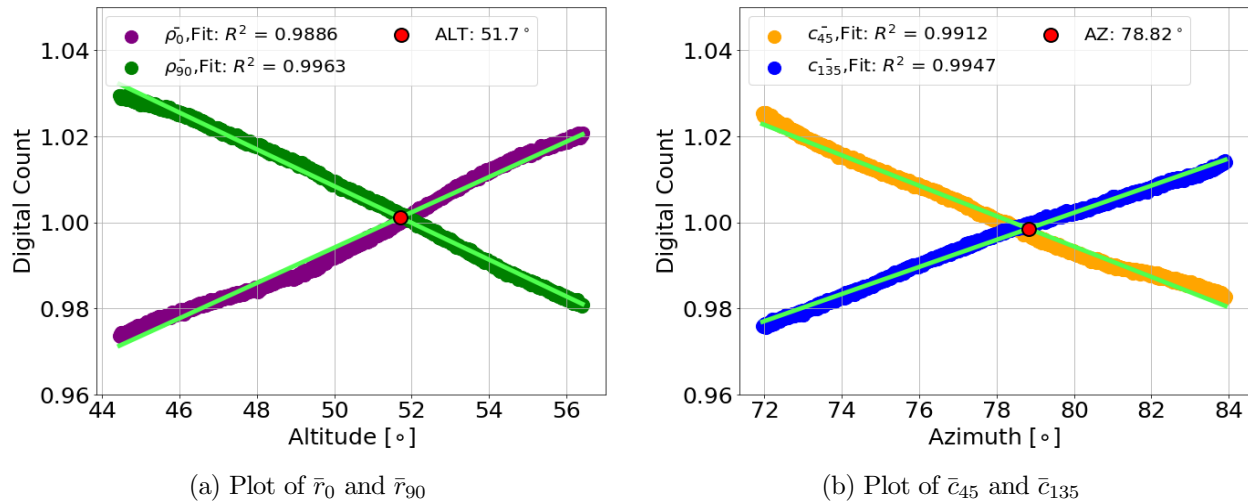
Figure 5: The linear fits are shown in bright green overlaid on the pixel values and the x-intercept is marked by the red dot. (a) $\bar{r}_0$ and $\bar{r}_{90}$ plotted over altitude (ALT) giving the neutral point ALT of $51.70°$. (b) $\bar{c}_{45}$ and $\bar{c}_{135}$ plotted over azimuth (AZ) giving the neutral point AZ of $78.82°$.

of $\bar{r}_0$ and $\bar{r}_{90}$ corresponds to the altitude of the neutral point, and the intersection of $\bar{c}_{45}$ and $\bar{c}_{135}$ corresponds to the azimuth, as shown in Figure 5. Altitude is measured from the horizon and azimuth is measured clockwise from cardinal south.

The neutral point location is estimated at an altitude of $51.70°$ ($22.06°$ above the Sun) within the range reported in the literature. The azimuth of the neutral point deviates from the expected literature value, wherein the neutral point and the Sun have equal azimuth coordinates. Specifically, the observed neutral point azimuth from ULTRASIP is $1.68°$ away from the azimuth of the Sun. This difference is most likely due to a combination of the Sun movement over the measurement time and uncertainties in the measurement pointing. The Sun is expected to move $0.0025°$ over the measurement time of 6 seconds for the four $P_\phi$ images or 4 pixels.

## Summary

Fundamental principles of atmospheric light scattering support the interest in polarization neutral points as markers for a wildfire smoke detection method that is not reliant on visual contact with the smoke plume. Imaging the neutral points relies on designing an optical system and estimation method for the neutral point's location in the sky. The demonstration of UTLTRSIP successfully imaging the Babinet neutral point is the first step toward polarization-enabled wildfire detection.

## References

[1]   O. V. Kalashnikova et al. "Photopolarimetric Sensitivity to Black Carbon Content of Wildfire Smoke: Results From the 2016 ImPACT-PM Field Campaign". In: *Journal Of Geophysical Research: Atmospheres* (2017). DOI: 10.1029/2017jd028032.

[2]   Clarissa M. DeLeon et al. "Polarimetric coordinate validation for merging GRASP and AirMSPI FIREX-AQ observations". In: *Journal of Quantitative Spectroscopy and Radiative Transfer* 317 (2024). DOI: https://doi.org/10.1016/j.jqsrt.2024.108910.

[3]   G. Horváth et al. In: *Polarized Light in Animal Vision*. Springer-Verlag Berlin Heidelberg, 2004.

[4]   M V Berry, M R Dennis, and R L Lee. "Polarization singularities in the clear sky". In: *New Journal of Physics* (2004). DOI: 10.1088/1367-2630/6/1/162. URL: https://dx.doi.org/10.1088/1367-2630/6/1/162.

[5]   C. Bellver. "Influence of particulate pollution on the positions of neutral points in the sky at Seville (Spain)". In: *Atmospheric Environment (1967)* 21.3 (1987), pp. 699–702. ISSN: 0004-6981. DOI: https://doi.org/10.1016/0004-6981(87)90051-5. URL: https://www.sciencedirect.com/science/article/pii/0004698187900515.

[6]   Hans Neuberger. "Arago's Neutral Point: A Neglected Tool in Meteorological Research". In: *Bulletin of the American Meteorological Society* 31.4 (1950), pp. 119–125. ISSN: 00030007, 15200477. URL: http://www.jstor.org/stable/26241629 (visited on 07/22/2024).

[7]   Clarissa M. DeLeon et al. "UV Linear Stokes Imaging of Optically Thin Clouds". In: (2021). SPIE Polarization Science and Remote Sensing.

[8]   Edward Collett. *Field Guide to Polarization*. SPIE Press, 2005.

[9]   Russell A. Chipman, Wai Sze Tiffany Lam, and Garam Young. *Polarized Light and Optical Systems*. CRC Press, 2018.

[10]  Craig F. Bohren and Donald R. Huffman. *Absorption and Scattering of Light by Small Particles*. WILEY-VCH Verlag GmbH & Co. KGaA, 1998.

[11]  Christoph von Friedeburg. "Derivation of Trace Gas Information Combining Differential Optical Absorption Spectroscopy with Radiative Transfer Modelling". PhD thesis. University of Heidelberg, 2003.

[12]  Scott Prahl. *MiePython: A Python Package for Mie Scattering Calculations*. https://miepython.readthedocs.io/en/latest/. Revision 0c188876, Licensed under the MIT License. 2024.

[13]  G. P. Konnen. *Polarized Light in Nature*. Cambridge University Press, 1985.

[14]    Zhiguo Fan et al. "Neutral point detection using the AOP of polarized skylight patterns". In: *Opt. Express* 4 (2021). DOI: `10.1364/OE.414718`.

[15]    Antoine Moutenet et al. "OpenSky: A Modular and Open-Source Simulator of Sky Polarization Measurements". In: *IEEE Transactions on Instrumentation and Measurement* (2024). DOI: `10.1109/TIM.2024.3374965`.

[16]    József Gál et al. "Polarization Patterns of the Summer Sky and Its Neutral Points Measured by Full-Sky Imaging Polarimetry in Finnish Lapland North of the Arctic Circle". In: *Proceedings: Mathematical, Physical and Engineering Sciences* 457.2010 (2001), pp. 1385–1399. ISSN: 13645021. URL: `http://www.jstor.org/stable/3067290` (visited on 11/13/2023).

[17]    David Peterson, Sarah Mccaffrey, and Toral Patel. *Wildland Fire Smoke in the United States A Scientific Assessment*. Springer, 2022. DOI: `https://doi.org/10.1007/978-3-030-87045-4`.

[18]    Clarissa M. DeLeon and Meredith K. Kupinski. "Development of a Sun-Tracking Linear Stokes Imaging Polarimeter". In: *Optical Design & Fabrication* (2024).

[19]    Meredith K. Kupinski et al. "Angle of linear polarization images of outdoor scenes". In: *Opt. Eng.* 58.8 (2019).